

Performance enhancement of a direct absorption solar collector using copper oxide porous foam and nanofluid

Mostafa Esmaeili¹  | Maryam Karami¹  | Shahram Delfani²

¹Faculty of Engineering, Kharazmi University, Tehran, Iran

²Department of Installations, Road, Housing and Urban Development Research Center (BHRC), Tehran, Iran

Correspondence

Mostafa Esmaeili, Faculty of Engineering, Kharazmi University, Tehran, Iran.
Email: m.esmaeili@khu.ac.ir

Summary

The current research proposes the idea of using water-saturated metal oxide foams and water-based nanofluids as solar absorber in the direct absorption solar collectors (DASCs). Specifically, the novel solar collector design utilizes copper oxide (CuO) porous foam and nanoparticle with high optical properties and is expected to have enhanced thermal performance than the conventional collectors utilizing pure water. The finite volume technique is used to solve the governing equations of flow and heat transfer in the radiative participating media. Also, to establish the reliability and accuracy of numerical solutions, the obtained results are compared with the corresponding numerical and experimental data. The computations are carried out for different nanoparticle volume fractions, foam pore sizes, working fluid mass flow rates, and both porous layer thicknesses and positions (inserted at the lower or upper wall of the collector). It is found that the efficiency of DASC partially/fully filled with metal oxide foam is maximized when the collector is completely filled with it. Compared with the water flow, the numerical results show that the collector efficiency using CuO nanofluid and metal oxide foam is improved by up to 26.8% and 23.8%, respectively. Moreover, considering the second law of thermodynamics, the use of CuO nanofluids in the DASC seems to be more effective than the use of CuO porous foam.

KEYWORDS

direct absorption solar collector, efficiency, metal oxide foam, nanofluid, second law of thermodynamics

1 | INTRODUCTION

The demand for energy production based on fossil fuel resources has had an increasing trend in recent years.¹ Due to the limitations of fossil fuel resources and associated environmental problems (CO emission increment), turning to renewable energy seems inevitable.² Among the various forms of renewable energy (including nuclear, solar, wind, ocean, and geothermal resources), the use of solar energy has numerous benefits such as environmental pollution reduction, high sustainability,

abundance, and low price. Solar energy can be harvested through photovoltaic cells or solar collectors.³ In various solar thermal collectors, including concentrating and non-concentrating collectors, the incoming solar radiation energy into the collector is converted to useful thermal energy.⁴ In conventional collectors, such as a flat plate solar collector (FPSC), the incident radiation heats the adsorbent plate and then a part of the heat is transferred to the carrier fluid. In contrast, in a direct absorption solar collector (DASC), the radiation is directly absorbed by the heat transfer fluid (HTF) and the solar energy is

converted into applied thermal energy.⁵ Since the optical characteristics (such as extinction coefficient) of HTF significantly influence the volumetric absorption process, these properties are more important in direct absorption collectors than the thermophysical ones. Due to the low extinction coefficient of common fluids (such as water), the addition of nanoparticles to the working fluid and placing open-cell metal oxide foam in direct absorption solar collectors (DASCs) can improve the extinction coefficient of HTF, thus increasing the collector efficiency.

The application of nanofluids in low-temperature DASCs has been the focus of various experimental and theoretical/numerical studies.⁶⁻²⁸ A comprehensive review of the subject is found in.²⁹⁻³¹ Gorji and Ranjbar²⁹ reviewed the optical properties and application of nanofluids in low and high heat flux DASCs. Among experimental studies, as pioneering research in this field, Otanicar et al²⁶ investigated the effect of adding nanoparticles (made of silver, carbon nanotube, and graphite) to water (as the base fluid) in a micro-DASC. They found that although the collector efficiency rises as the volume fraction of nanoparticles increases, the efficiency slightly decreases beyond a certain volume fraction. The effect of adding aluminum oxide nanoparticles (with a diameter of 20 nm) to the water with different volume fractions was investigated by Gupta et al.²² They reported a maximum enhancement of 39% in the instantaneous collector efficiency for a 0.005% volume fraction. In a similar experimental set-up, the effects of bottom wall optical conditions (black or reflective wall) and the volume fractions of graphene nanoparticles in different mass flow rates were studied by Karami et al²⁴ and Vakili et al,²⁷ respectively. In a recent study, Karami et al³⁰ investigated the energy and exergy efficiencies in a DASC in which the effect of V-shaped rib roughness in DASC bottom is considered. Two rib configurations, namely forward (FR) and backward (BR) DASCs, and various graphene oxide nanofluid concentrations and mass flow rates were considered in their experiment. They concluded that the zero-loss efficiency for FR and BR rib geometries, compared to conventional collectors, increases by 21% and 13.4%, respectively. Additionally, it was found that adding 500 ppm of graphene nanoparticles to the base fluid maximizes energy and exergy efficiencies of FR and conventional collectors. Among numerical studies, Tyagi et al¹⁷ concluded that using water-aluminum nanofluid leads to 10% more efficiency in DASC than in FPSC (under the same conditions). Using the finite element method, the effects of volume fraction and diameter of copper nanoparticle, solar heat flux and Prandtl number on the thermal efficiency and entropy generation in a DASC were studied by Nasrin et al.² Moradi et al³² conducted an analytic

three-dimensional study on the flow and heat transfer along with the optical ray-tracing model in a direct absorption tube collector containing carbon nanotubes. They showed that the collector efficiency in water-based nanofluids is higher than that in glycol-based nanofluids.

Using a transient one-dimensional model, Duan et al⁶ evaluated the photo-thermal efficiency of a DASC containing SiO₂/Au nanofluids. They found that the collector efficiency is significantly increased using plasmonic nanoshell-based nanofluid with an optimum collector depth of 10 mm. Siavashi et al¹⁶ evaluated the effect of the presence (and position) of an absorber plate in a DASC filled with single-walled carbon nanohorns (SWCNH) using the lattice Boltzmann method. They concluded that placing the absorber plate, especially for water flow, remarkably increases the collector efficiency. Moreover, the maximum efficiency is achieved when the metal sheet is located on the collector floor. More recently, Sharaf et al¹³ numerically investigated the balance between power gain (as a quantitative parameter of collector output) and temperature gain (as a qualitative parameter of collector output) in a nanofluid-based DASC. Using a constrained multivariable global optimization method, they showed that exergy efficiency begins to decrease at a certain amount of thermal efficiency (55%).

Employing porous materials is a common method to improve the heat transfer characteristics of solar energy systems. Rashidi et al³³ reviewed various applications of porous materials in solar energy systems. Porous media including metal foams and porous metals can be used to augment the volumetric absorption of solar radiation in direct absorption collectors due to their high extinction coefficient. In general, benefiting from porous materials with high thermal conductivity can lead to increased heat mixing, resulting in increased heat transfer rate and better efficiency in solar collectors (non-direct radiation absorption through the surface absorber). To enhance the heat transfer using porous media, numerous numerical and experimental studies have focused on the use of porous materials in flat plate³⁴⁻⁴¹ and parabolic^{42,43} collectors. For instance, Saedodin et al⁴⁰ experimentally and numerically examined the effect of metallic foam (partially/totally filled) on the performance of an FPSC. Their numerical model showed that the optimal dimensionless thickness of the metal foam layer is greater than 0.8. Furthermore, they concluded that the maximum improvement in collector efficiency and Nusselt number due to the use of metal foam is 18.5% and 85%, respectively. The influence of metal foam insert as a passive tool for improving heat transfer in an FPSC was evaluated by Javaniyan Jouybari et al.³⁷ Their calculations showed that by increasing the Reynolds number, the overall collector

performance, as a parameter that takes both pressure drop and Nusselt number into account, decreases. Also, despite the rise in the pressure drop in a metal foam-filled channel, the effect of entropy generated by heat transfer is much greater than that generated by pressure drop. Jamal-Abad et al.⁴³ investigated the efficiency of a parabolic trough collector (PTC) whose absorber is filled by copper metal foam (with a porosity of 0.9 and pore diameter of 30 PPI). It was found that using metal foam, the overall loss coefficient decreases by 45%, thereby improving the collector efficiency. In a recent study, Anirudh and Dhinakaran³⁴ numerically studied the effect of metal foam blocks on the efficiency of an FPSC. Their results showed that as the number and height of the porous blocks increase, despite the notable improvement in heat transfer, the pressure drop increases as a negative consequence. Moreover, the collector performance parameter improves when the number of metal foam blocks is minimal and the foam layer height is less.

An essential component of PTCs is the thermal receiver in which the radiation energy is converted to thermal energy.⁴⁴⁻⁴⁶ To increase the solar energy absorption and subsequently increase the collector efficiency as well as outlet temperature, a volumetric receiver can be equipped with porous matrix. Numerous studies have investigated the efficiency of porous volumetric receivers.^{44,47-49} It should be noted that in most of them, air and ceramic foams are used as the HTF and porous media, respectively. Few studies have considered the volumetric receiver occupied by a liquid saturated metal foam.^{50,51} Recently, Valizade et al.⁵¹ investigated the application of copper metal foam in a direct absorption PTC at different mass flow rates, inlet temperatures, and porous insert configurations. It is found that using the full porous configuration, the efficiency of the collector increases by up to 171% compared to the porous-free tube. However, to the best of our knowledge, there has been no experimental or numerical study on the evaluation and application of

metal oxide foam in the non-concentrating DASCs. To this aim, the use of copper oxide (CuO) porous foam in a DASC (partially/fully filled with porous foam) is numerically addressed and the efficiency and entropy generation of the collector in this case is compared with those of DASC containing CuO nanofluid. Additionally, in numerical simulations, the optical properties of water-saturated CuO porous foam and water/CuO nanofluids are considered based on the experimental study of Valizade et al.⁵² and the guidelines reported by Dugaria et al.⁵

2 | MATHEMATICAL FORMULATION AND COMPUTATIONAL SETUP

2.1 | Problem description

The dimensions of the DASC used in the present study, is based on the experimental study of the Karami²³. As schematically illustrated in Figure 1A, the length and width of the collector is 60 cm ($W = L = 60$ cm) and its height is 1 cm ($H = 1$ cm). The main body and top surface of the collector are made of aluminum and a 4 mm glass (with a 90% passing ratio), respectively. Also, the whole solar collector except its upper surface is well insulated and the internal surface of the lower wall is a perfect absorptive. The full details of the experimental set up are available in the Reference 23. Given that $W > 10 H$, the two-dimensional flow assumption is valid for this collector. The two-dimensional computational domain is shown in Figure 1B. The solar radiation is absorbed by nanoparticles or metal oxide foam, and the absorbed radiation generates a volumetric heat and thereby increases the temperature of the fluid. As shown, the HTF enters the channel with a constant temperature (T_{in}) and a uniform velocity (U_{in}). The upper boundary of the collector is considered to be a semitransparent wall

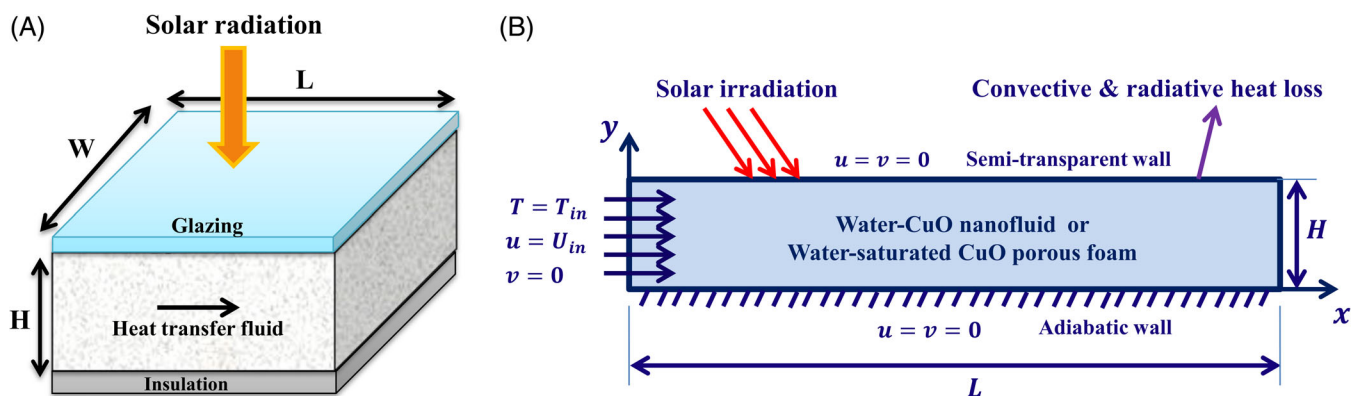


FIGURE 1 Schematic of direct absorption solar collector, (A) 3D view (B) computational domain [Colour figure can be viewed at wileyonlinelibrary.com]

which is exposed to the sun's radiation flux, while also allowing heat exchange with the surrounding through convection and radiation.

The two dimensional, laminar flow computations in this study are presented in two parts. In the first part, the nanofluid flow, produced by adding CuO nanoparticles to the water as the base-fluid, through the collector is simulated. It is assumed that the temperature of the fluid and the nanoparticles are the same and the nanofluid is modeled as a single-phase homogeneous material.^{53,54} In nanofluid computations, the volume fraction of CuO nanoparticles is considered to be 0.01%, 0.05%, and 0.1%. In the second part, we investigate the water flow inside the DASC occupied by the CuO porous foam as a solar absorber material. In the present study, metal oxide foam is considered as a homogeneous and isotropic medium with uniform porosity and permeability. Also, it is assumed that there is a local heat equilibrium (LTE) between the metal oxide foam and the water and the metal oxide foam matrix is completely saturated with water.³⁴ In porous foam simulations, the effect of the porous foam layer thickness and its inserted position (upper or lower wall of the DASC channel) are studied. Moreover, it is worthy to note that both series of simulations (nanofluid flow and flow in porous foam-filled channel) are performed at the mass flow rates of 0.0075, 0.015, and 0.0225 kg/s and a solar radiation fluxes (G_T) of 800 W/m².

2.2 | Governing equations

Here, the governing equation of the two-dimensional steady laminar nanofluid flow through DASC and also, water flow inside DASC partially/fully filled with metal oxide foam is presented. The mass, momentum, and energy conservation equations of nanofluid, modeled as a single-phase isotropic fluid, can be expressed as.

$$\frac{\partial u_i}{\partial x_i} = 0, \quad (1)$$

$$\rho_{nf} \frac{\partial (u_j u_i)}{\partial x_j} = -\frac{\partial p}{\partial x_i} + \mu_{nf} \left(\frac{\partial^2 u_i}{\partial x_j \partial x_j} \right), \quad (2)$$

$$\rho_{nf} C_{p,nf} \frac{\partial (u_j T)}{\partial x_j} = \frac{\partial}{\partial x_j} \left(k_{nf} \frac{\partial T}{\partial x_j} \right) + S, \quad (3)$$

where p is the pressure, u_i is the velocity vector component in stream-wise and transverse directions, and T is the temperature. The density, viscosity, thermal conductivity, and heat capacity of the nanofluid are respectively denoted by ρ_{nf} , μ_{nf} , k_{nf} , and $C_{p,nf}$.

The momentum equation for the water-saturated metal oxide foam is expressed based on the Brinkman–Forchheimer-extended Darcy model that incorporates both viscous and inertia effects. The governing equations (momentum and energy) for the flow and heat transfer through porous foam are given as follows:

$$\frac{\rho}{e} \frac{\partial (u_i)}{\partial x_j} = -\frac{\partial p}{\partial x_i} + \frac{\mu}{e} \left(\frac{\partial^2 u_i}{\partial x_j \partial x_j} \right) - f \left[\frac{\mu}{K} u_i + \rho_f K^{-1/2} (C_F u_i |u_j|) \right], \quad (4)$$

$$\rho_f C_p \frac{\partial (u_j T)}{\partial x_j} = k_{eff} \left(\frac{\partial^2 T}{\partial x_j \partial x_j} \right) + S, \quad (5)$$

where, ρ , C_p , and μ are the density, heat capacity, and viscosity of the fluid (water in this study). The f and e indices in Equation 4 specify the porous and fluid regions as follows⁵⁵:

$$\begin{cases} \text{For porous region } f = 1, & e = \varepsilon \\ \text{For fluid region } f = 0, & e = 1 \end{cases}. \quad (6)$$

In the above equations, ε and K are the porosity and permeability of the porous media. The inertia coefficient of the porous media, C_F , can be computed according to the following equation.⁵⁶

$$C_F = \frac{1.75}{\sqrt{150\varepsilon^{3/2}}}. \quad (7)$$

Also, the effective thermal conductivity of the porous media in terms of fluid and solid thermal conductivities (k_f and k_s) is defined as follows:

$$k_{eff} = \varepsilon k_f + (1 - \varepsilon) k_s. \quad (8)$$

The energy equation source terms in Equation 3 (nanofluid flow) and Equation 5 (flow in porous media) S , is the volumetric heat source due to radiation in participating media (nanoparticles and metal oxide foam) which is expressed as⁵

$$S = \int_0^\infty a_\lambda \left(\int_0^{4\pi} I_\lambda(\lambda\omega) d\omega \right) d\lambda - 4\pi \int_0^\infty a_\lambda I_{b\lambda}(\lambda) d\lambda, \quad (9)$$

where I_λ and a_λ are the radiation intensity and spectral absorption coefficient respectively. Moreover, $I_{b\lambda}$ is the spectral blackbody intensity which is determined using the Planck's blackbody relation.¹⁸ In order to compute the radiation intensity, one should solve the radiative transfer equation (RTE) in which the radiation energy interaction with the participating media under the influence of absorption, emission and scattering processes is

mathematically described. The RTE for location \vec{r} and direction \vec{s} is defined as follows:

$$\frac{dI_\lambda(\vec{r}, \vec{s})}{d\vec{s}} + (a_\lambda + \sigma_\lambda)I_\lambda(\vec{r}, \vec{s}) = a_\lambda I_{b\lambda}(T, \vec{r}, \vec{s}) + \frac{\sigma_\lambda}{4\pi} \int_0^{4\pi} I_\lambda(\vec{r}, \vec{s}') \Phi(\vec{s}, \vec{s}') d\omega, \quad (10)$$

where, σ_λ , \vec{s}' , Φ , and ω are the spectral scattering coefficient, scattering direction, scattering phase function, and solid angle, respectively. In the present study, an isotropic scattering phase function is applied. In addition, the contribution of scattering coefficient to the total extinction coefficient for the nanofluid flow is ignored¹⁸ and for the metal oxide foam, it is obtained base on the proposed equation by Vafai.⁵⁷ As will be explained later in the material properties section, based on the experimental data obtained by Valizadeh et al⁵² the spectral absorption coefficient is calculated.

The corresponding boundary conditions for solving the momentum and energy equations are given as:

$$\begin{aligned} & @ x = 0, u = U_{in}, v = 0 \ \& \ T = T_{in} \\ & @ x = L, p = 0 \\ & @ y = 0, u = v = 0 \ \& \ \left(\frac{\partial T}{\partial y}\right)_{y=0} = 0 \\ & @ y = H, u = v = 0 \ \& \ \left(k_{nf} \frac{\partial T}{\partial y}\right)_{y=0} = h_c(T_{y=h} - T_\infty) \\ & \quad \quad \quad + h_r(T_{y=h} - T_{sky}) \text{ for nanofluid} \\ & @ y = H, u = v = 0 \ \& \ \left(k_{eff} \frac{\partial T}{\partial y}\right)_{y=0} = h_c(T_{y=h} - T_\infty) \\ & \quad \quad \quad + h_r(T_{y=h} - T_{sky}) \text{ for metal oxide foam.} \end{aligned} \quad (11)$$

Furthermore, in order to ensure continuity of the velocity, temperature, pressure, shear stress, and heat flux at the metal oxide foam and fluid regions interface, the following conditions must be satisfied⁵⁸:

$$\begin{aligned} (u_i)_f &= (u_i)_{mf} \\ (T)_f &= (T)_{mf} \ \& \ \left(k_{eff} \frac{\partial T}{\partial y}\right)_f = \left(k_{eff} \frac{\partial T}{\partial y}\right)_{mf} \\ \left(\frac{\partial u}{\partial y} + \frac{\partial v}{\partial x}\right)_f &= \frac{1}{\varepsilon} \left(\frac{\partial u}{\partial y} + \frac{\partial v}{\partial x}\right)_{mf} \\ \left(\frac{\partial v}{\partial y}\right)_f &= \frac{1}{\varepsilon} \left(\frac{\partial v}{\partial y}\right)_{mf} \end{aligned} \quad (12)$$

where 'f' and 'mf' subscripts refer to fluid and metal oxide foam regions, respectively. The boundary conditions used for the RTE equation are similar to that outlined by^{18,59,60} Here, by determining the governing equations and

boundary conditions, the parameters required for the post-processing are presented. An important criterion for determining the thermal performance of a collector is the 'thermal efficiency' in which the ratio of the useful thermal energy to the incoming solar energy is calculated as follows²:

$$\eta_{th} = \frac{\dot{m}C_p(T_{out} - T_{in})}{G_T A_c}, \quad (13)$$

where T_{out} and A_c are the outlet temperature and area of the collector, respectively.

The entropy generation in a solar collector can be due to the irreversibility caused by the heat transfer and the fluid flow friction. According to the procedure proposed by Bejan,⁶¹ the rate of local entropy generation per unit volume is calculated based on the following equation:

$$S'''_{gen} = S'''_{gen,H} + S'''_{gen,F}. \quad (14)$$

$S'''_{gen,H}$ is the entropy generation due to the limited temperature difference that results in heat transfer and is calculated by the following equation:

$$\begin{aligned} S'''_{gen,H} &= \frac{k_{nf}}{T_{in}} \left(\left|\frac{\partial T}{\partial x_j}\right|\right)^2 \text{ for nanofluid} \\ S'''_{gen,H} &= \frac{k_{eff}}{T_{in}} \left(\left|\frac{\partial T}{\partial x_j}\right|\right)^2 \text{ for metal oxide foam.} \end{aligned} \quad (15)$$

$S'''_{gen,F}$ is the entropy generation by the velocity gradient, which leads to friction and pressure drop in the flow. For the nanofluid flow and water flow in the nonporous region (in the channel partially filled with porous material), $S'''_{gen,F}$ is calculated from the following relation:

$$S'''_{gen,F} = \frac{\mu}{T_{in}} \left(\frac{\partial u_i}{\partial x_j} + \frac{\partial u_j}{\partial x_i}\right) \frac{\partial u_i}{\partial x_j}. \quad (16)$$

For the water flow in the nonporous region of the channel, the μ is the water viscosity, and for the nanofluid flow that is μ_{nf} . The amount of entropy generated by the flow friction in a porous region is written as follows⁵⁵:

$$S'''_{gen,F} = \frac{\mu}{T_{in}} \left(\frac{\partial u_i}{\partial x_j} + \frac{\partial u_j}{\partial x_i}\right) \frac{\partial u_i}{\partial x_j} + \frac{\mu}{KT_{in}} u_i u_i + \frac{C_F}{KT_{in}} u_i u_i |u_j|. \quad (17)$$

If the collector volume is represented by V , the total entropy generation rate is obtained by integrating the Equation 14 over the whole computational domain. This

quantity in the dimensionless form, entropy generation number, can be expressed as follows⁶²:

$$N_s = \frac{\int S_{\text{gen}}''' dV}{\frac{G^2}{k_f T_{\text{in}}^2} V}. \quad (18)$$

Additionally, the dimensionless Bejan number, which represents the ratio of the heat transfer contribution in entropy generation to the total entropy generation caused by the heat transfer and flow friction, is defined as follows:

$$\text{Be} = \frac{\int S_{\text{gen},T}''' dV}{\int S_{\text{gen}}''' dV}. \quad (19)$$

2.3 | Solution methodology

In the present study, we rely on the finite volume method to solve the governing equations (ie, Equations 1–12). Due to the possibility of simulating a semitransparent wall (upper surface of the DASC), no limitation on the optical thickness of the material participating in the radiation, and the moderate computational cost in the usual angular discretization, discrete ordinate (DO) model is adopted to solve the radiation transfer equation. The RTE is converted to a transport equation for the radiation intensity in the spatial coordinates by using this model. In this study, a non-gray implementation of the DO model is used in which the radiation spectrum is divided into a finite number of wavelength bands, while in each band the gray radiation is assumed. The second-order upwind method is employed to discretize the convection fluxes in momentum, energy, and DO model equations. Using this method, both the stability and accuracy of the solution can be taken into account. Moreover, the diffusion terms are approximated by second-order central differences. Since there is no independent equation in the incompressible flow for obtaining the pressure field, SIMPLE algorithm is used to derive the pressure correction equation from the continuity equation and to create a coupling between velocity and pressure fields. The convergence criterion of the numerical solution is considered to be less than $1e-7$ for the residual error of the governing equations.

2.4 | Material properties

Here, the thermophysical and optical properties used in nanofluid and metal oxide foam computations are discussed. Assuming that the nanoparticles are small

enough to be homogeneously dispersed by the colloidal forces and that there is a thermal equilibrium between the nanoparticles and the base fluid, the nanofluid is considered to be a homogeneous single-phase medium.⁵³ Hence, the nanofluid density (ρ_{nf}) and specific heat ($C_{p_{\text{nf}}}$) can be expressed as follows:

$$\rho_{\text{nf}} = (1-\phi)\rho_b + \phi\rho_p, \quad (20)$$

$$C_{p_{\text{nf}}} = \frac{(1-\phi)(\rho C_p)_b + \phi(\rho C_p)_p}{(1-\phi)\rho_b + \phi\rho_p}, \quad (21)$$

where ϕ is the nanoparticle volume fraction. Also, assuming spherical nanoparticles, the thermal conductivity and viscosity of nanofluids (k_{nf} and μ_{nf}) can be calculated from the classical Maxwell Garnett (MG)⁶³ and Brinkman⁶⁴ models as follows:

$$\frac{k_{\text{nf}}}{k_b} = \frac{k_p + 2k_f - 2(k_f - k_p)\phi}{k_p + 2k_f + (k_f - k_p)\phi}, \quad (22)$$

$$\mu_{\text{nf}} = \frac{\mu_f}{(1-\phi)^{2.5}}. \quad (23)$$

In Equations 20–23, the subscripts ‘p’, ‘b’, and ‘nf’ respectively denote the nanoparticle, base-fluid, and nanofluid. The viscosity and thermal conductivity of nanofluid is also computed using different well-known correlations (the nanofluid viscosity models of Einstein,⁶⁵ Batchelor,⁶⁶ and Wang⁶⁷) as well as some other empirical correlations,^{68–72} which are functions of both temperature and volume fraction, while no significant change was observed in the obtained results. This can be attributed to the low concentration of nanoparticles and the low-temperature variations in the DASC. Thermophysical properties of CuO nanoparticles and water as the base fluid, required in Equations 20–23, are listed in Table 1. As mentioned earlier, to compare the thermal performance of the thermal collector using nanoparticles and porous media, the CuO porous foam (made of nanoparticle-like material) is employed. Table 2 presents the specifications of the CuO porous foam used in the computations.⁵²

One of the most important steps in numerical simulation of the radiation heat transfer in participating media is to determine their optical properties. The optical properties of the radiation absorbers have an important influence on the thermal performance of the volumetric solar collectors. In the present study, the optical properties required for numerical modeling of DASC are used based on a recent study of Valizadeh et al.⁵² For this purpose,

TABLE 1 Thermophysical properties of the pure water and CuO nanoparticle at $T = 300$ K

	Density (kg/m ³)	Specific heat (J/kgK)	Thermal conductivity (W/mK)	Viscosity (Ns/m ²)	Diameter
Water	997.1	4179	0.613	0.0010003	–
CuO nanoparticle ⁷⁷	6500	540	18	–	30 nm

similar to the procedure discussed by Dugaria⁵ for the non-gray radiation modeling, the spectral distribution of the optical properties of participating media (CuO nanoparticles CuO porous foam) in the wavelength range from 300 to 1700 nm is divided into different size bands. It is assumed, the optical properties within each band are constant and radiation is gray.

3 | RESULT AND DISCUSSION

In this section, the numerical solution results are discussed. First, the grid independency as well as the numerical validation is discussed. The proposed numerical solution is validated using the numerical investigation of two different experimental studies on nanofluid flow in DASC^{23,26} and the obtained collector efficiency is compared with the experimental data. Next, the flow and heat transfer in a channel filled with porous media are simulated and the obtained Nusselt number and pressure drop are compared with the corresponding numerical results.⁷³ After ensuring the validity of the numerical method, the numerical results of the CuO-water nanofluid flow in DASC are presented and the effect of mass flow rate and nanoparticle concentration on the collector efficiency, and entropy and Bejan numbers are addressed. Finally, the water flow through DASC partially/fully filled with CuO porous foam is simulated and the effects of porous foam thickness and position in the collector and pore diameter in addition to the impacts of water mass flow rate on the flow, thermal efficiency, and entropy generation are investigated.

3.1 | Grid independency test and validation

In this study, a structured mesh is generated in the computational domain. To achieve a mesh-independent solution, the computations are performed using three grid sizes (coarse, medium, and fine). The computational grid is clustered near the walls to properly capture the velocity and temperature gradients. The grid independency test is carried out for nanofluid flow with a volume fraction of

TABLE 2 Characteristics of CuO porous foam used in calculations⁵²

Porosity (%)	Number of pores within an inch (PPI)
90	10
90	20
90	30

0.1% and for the flow in the porous foam-filled collector with PPI = 30. In both simulations, the mass flow rate is set to 0.0075 kg/s. To quantitatively evaluate the grid independency, the grid convergence index (GCI) is computed as proposed by Roache⁷⁴ and Celik et al⁷⁵ and employed in recent numerical studies.^{34,59} The GCI is based on Richardson extrapolation method, in which the obtained discrete numerical results from two different grids are compared. In the present study, the wall heat flux and shear stress at the output section of collector are calculated for the fine, medium and fine grids (f_1 , f_2 , and f_3 , respectively). The GCI for the medium grid with respect to the fine grid is defined as

$$GCI^{12}(\%) = \frac{F_S e_a^{12}}{(r_{12})^p - 1}, \quad (24)$$

where the constant values of 1.25 and 1.5 are considered for the factor of safety (F_S) and the grid refinement ratio (r), respectively. Moreover, the relative error of the discrete solutions obtained from the medium and fine grids (e_a^{12}) and the apparent order of convergence (p) are defined as

$$e_a^{12}(\%) = \frac{f_2 - f_1}{f_1} \times 100, \quad (25)$$

$$p = \frac{\ln\left(\frac{f - f_2}{f_2 - f_1}\right)}{\ln(r_{12})}. \quad (26)$$

Similarly, the GCI for the coarse grid with respect to the medium grid (GCI^{23}) is obtained. In Table 3, the GCI of the medium grid relative to the fine grid and that of the coarse grid relative to the medium grid are calculated

for the wall heat flux and shear stress. As shown in Table 3, a decrease in the GCI values is observed ($GCI^{23} < GCI^{12}$). Moreover, based on Richardson extrapolation, with a GCI of less than 5%, a-grid independent solution is achieved. Therefore, all three grids are applicable for the computations, but since the values obtained for medium and fine grids are so close to each other (small relative error), the medium grid is the most desirable one and is, therefore, chosen for further simulations.

Three different cases are chosen to validate the numerical solutions. In the first case, the experimental

and numerical study of Otanicar et al²⁶ is investigated. They considered the graphene/water nanofluid flow through DASC at 42 mL/h and the solar radiation flux of 1000 W/m². In Figure 2A, DASC thermal efficiency at different nanoparticle volume fractions (from 0% to 0.1%) obtained from numerical results are compared with experimental and numerical results of Otanicar et al.²⁶ A good agreement is observed between the results, especially at lower nanoparticle volume fractions. In the second case of validation, a recent experimental study of Karami²³ is considered. The energy and exergy

TABLE 3 Grid independency checks for nanofluid and water-saturated metal oxide foam simulations

GRID $N_x \times N_y$	Nanofluid				Metal oxide foam			
	q''_{max}	GCI(%)	$\tau_{w, max}$	GCI(%)	q''_{max}	GCI(%)	$\tau_{w, max}$	GCI(%)
Coarse grid 600 × 60	406.974	0.142	0.000739	0.22	465.931	0.051321	0.006365	1.482205
Medium grid 900 × 90	403.848	0.018	0.000754	0.017	465.391	0.013445	0.006795	0.207049
Fine grid 1350 × 135	403.444	–	0.000755	–	465.250	–	0.006860	–

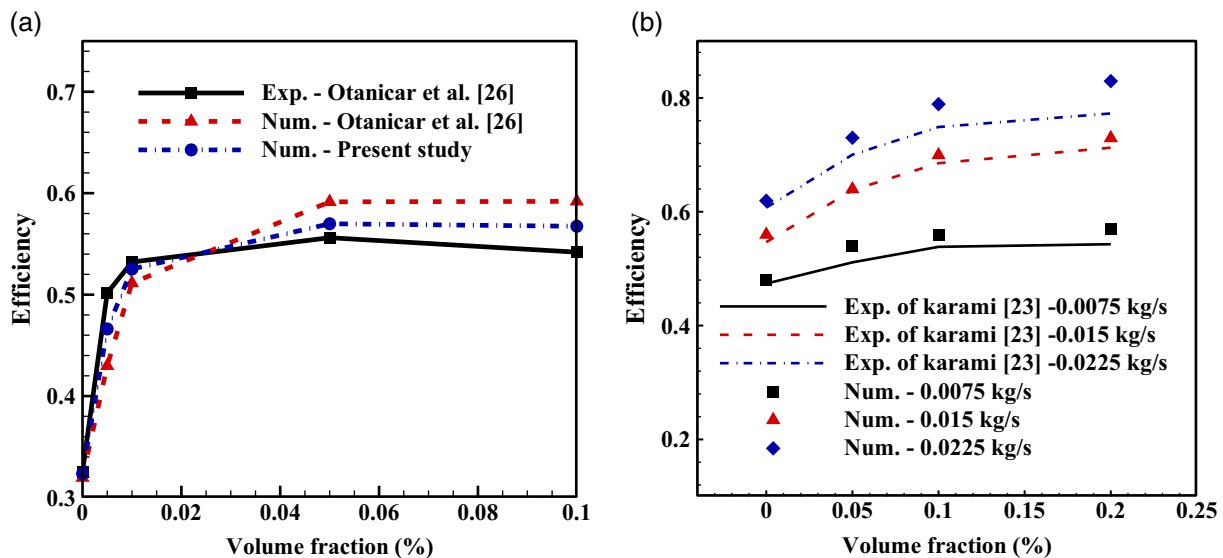


FIGURE 2 Comparison of the computed collector efficiency in the present study with the (A) experimental and numerical results of Otanicar et al²⁶ and (B) experimental data of Karami²³ [Colour figure can be viewed at wileyonlinelibrary.com]

TABLE 4 Comparison of predicted values of Nusselt number and pressure drop with the numerical results of Mohammad⁷³ for empty and porous-filled channel

	Local Nu number (present study)	Local Nu number (Mohammad ⁷³)	Error (%)	Pressure drop per unit length (present study)	Pressure drop per unit length (Mohammad ⁷³)	Error (%)
Water	7.42	7.541	1.604	0.0295	0.03	1.666
Porous filled channel	9.54	9.772	2.374	98.03	101	2.940

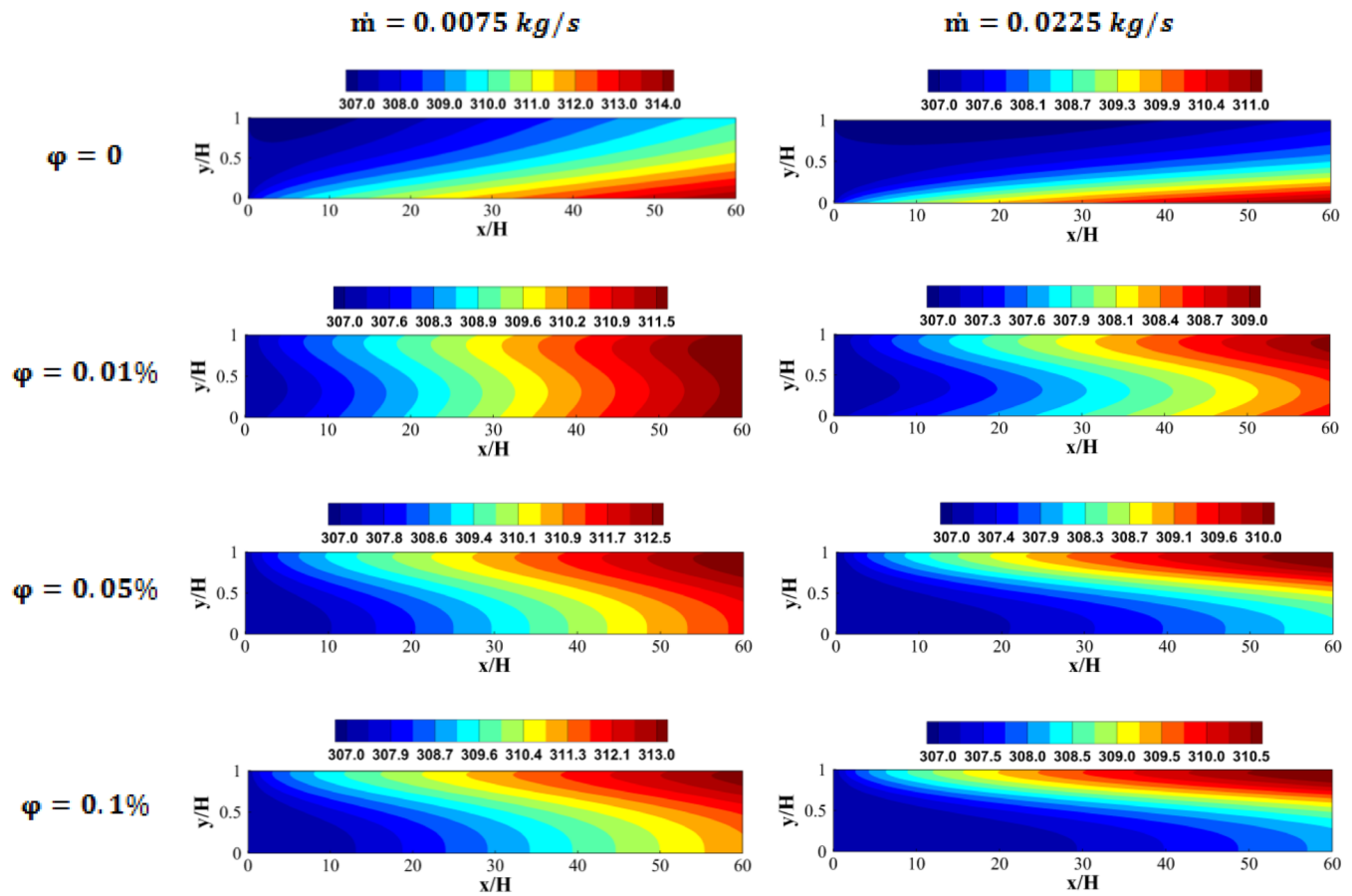


FIGURE 3 Temperature contour at different nanoparticle volume fractions and two mass flow rates [Colour figure can be viewed at wileyonlinelibrary.com]

performance of $\text{Fe}_3\text{O}_4/\text{SiO}_2/\text{water}$ nanofluid flow at the mass flow rates of 0.0075, 0.015, and 0.0225 kg/s were investigated in a residential-type DASC²³. In the current study, the optical properties of nanofluid at different nanoparticle concentrations required for numerical modeling are derived from experimental data.²³ Figure 2B compares the computed collector efficiency at different mass flow rates and volume fractions with experimental data²³ and a reasonable agreement is obtained. Similar to the first validation case, the maximum deviation between numerical and experimental results is related to the thermal efficiency at the highest nanoparticle volume fraction. This discrepancy may be attributed to the single-phase modeling of CuO/water nanofluid mixture, assumption of constant solar heat flux and semitransparent modeling of glass cover. To validate the numerical method in water-saturated metal oxide foam modeling, no systematic experimental data have been found to simulate residential-type DASC filled with porous foam. Hence, the convection heat transfer through a channel filled with porous media is chosen as the third validation case and the obtained results are compared with the numerical results of Mohammad.⁷³

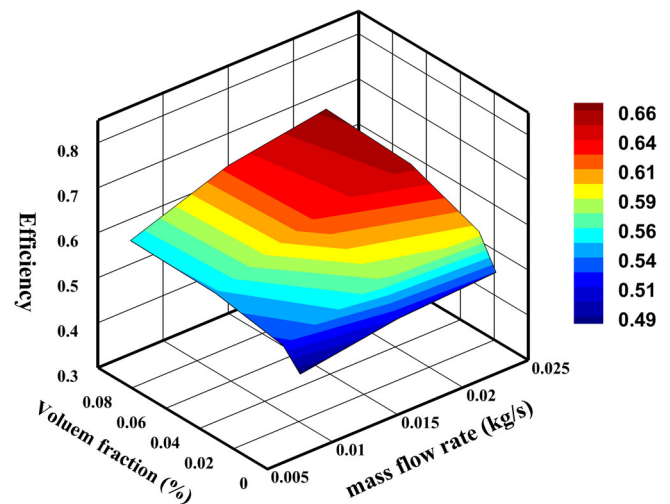


FIGURE 4 Collector efficiency for different nanofluid mass flow rates and nanoparticle volume fractions [Colour figure can be viewed at wileyonlinelibrary.com]

As presented in Table 4, the computed Nusselt number at the upper wall and the pressure drop per channel length for the porous-filled and empty channels are compared with the published numerical results.⁷³ The agreement

between the results of present study and the numerical findings of Muhammad⁷³ is acceptable with a difference of less than 3%.

3.2 | Performance of DASC filled with CuO nanofluids

In this section, the effect of nanofluid mass flow rate and volume fraction on DASC efficiency and entropy generation is investigated. The solar radiation flux is set to 800 W/m^2 . Figure 3 illustrates the temperature distribution in DASC for different CuO volume fractions and two mass flow rates. As mentioned earlier, the inner surface of the bottom wall is a complete absorber of radiation. Therefore, when the water flows into the collector, due to its low absorption coefficient, the incoming radiation passes through the water and is absorbed by the lower wall of the collector, thereby increasing the temperature of the fluid layer adjacent to the bottom wall. As the nanoparticles concentration increases, the nanofluid ability to absorb the solar radiation increases and the incoming radiation to the collector is absorbed by the nanofluid before reaching the lower wall. As shown in Figure 3, at $\phi = 0.01\%$, the temperature difference between the upper and lower walls of the collector is lower than for the other volume fractions and in these cases, the temperature profile seems more uniform (especially at larger x positions). The higher the concentration of nanoparticles, the higher the nanofluid absorption coefficient. As a result, the temperature of the fluid layers near the upper wall increases and the uniformity of the temperature profile vanishes. By increasing the mass flow rate from 0.0075 to 0.0225, the

residence time of fluid decreases¹⁸ and the incoming radiation to the collector is absorbed by the upper layers of the fluid, resulting in the fluid not having sufficient time to conduct heat to the lower layers. Accordingly, a high-temperature region is formed near the top wall. Furthermore, similar to the temperature distribution of 0.0075 kg/s , at the mass flow rate of 0.0225 kg/s , a volume fraction rise leads to increased maximum temperature in adjacent fluid layers with the upper wall. In Figure 4, the collector efficiency for different values of nanofluid mass flow rate and nanoparticle concentration is shown in a three-dimensional contour plot. It is readily observed that the average fluid temperature increases with the addition of nanoparticles to water due to a rise of the nanofluid absorption coefficient, thereby improving collector efficiency. For nanofluids with a volume fraction of 0.05% compared to nanofluids with a zero volume fraction (water), at the mass flow rates of 0.075 , 0.015 , and 0.025 kg/s , the DASC efficiency is improved by 13% , 21% , and 24% , respectively. A notable asymptotic behavior is observed for the collector efficiency variations with increasing nanoparticle concentration, such that the efficiency improvement by changing the volume fraction from 0.05% to 0.1% in different mass flow rates is about 1% . As discussed by Delfani et al,¹⁸ with increasing nanoparticle concentration, the temperature of the fluid layers adjacent with the collector upper wall also rises. This results in increased heat loss to the environment through convection and radiation heat transfer. Furthermore, as seen in Figure 4, at a constant volume fraction, the collector efficiency increases with increasing mass flow rate. This can be attributed to a growth in the amount of heated nanofluid mass over a specific period.¹⁶

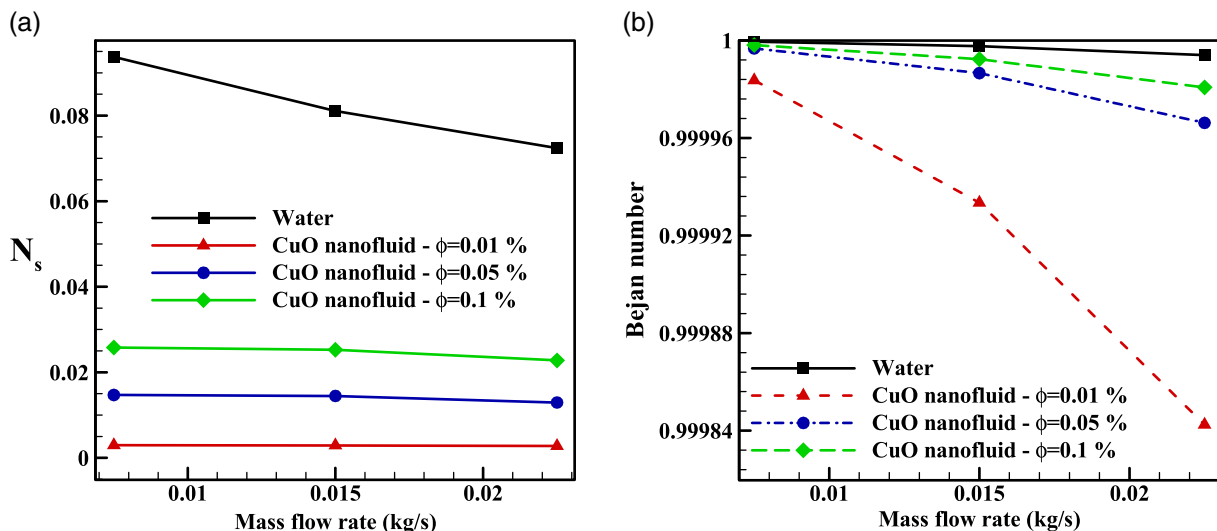


FIGURE 5 (A) Entropy generation number and (B) Bejan number for different nanofluid mass flow rates and nanoparticle volume fractions [Colour figure can be viewed at wileyonlinelibrary.com]

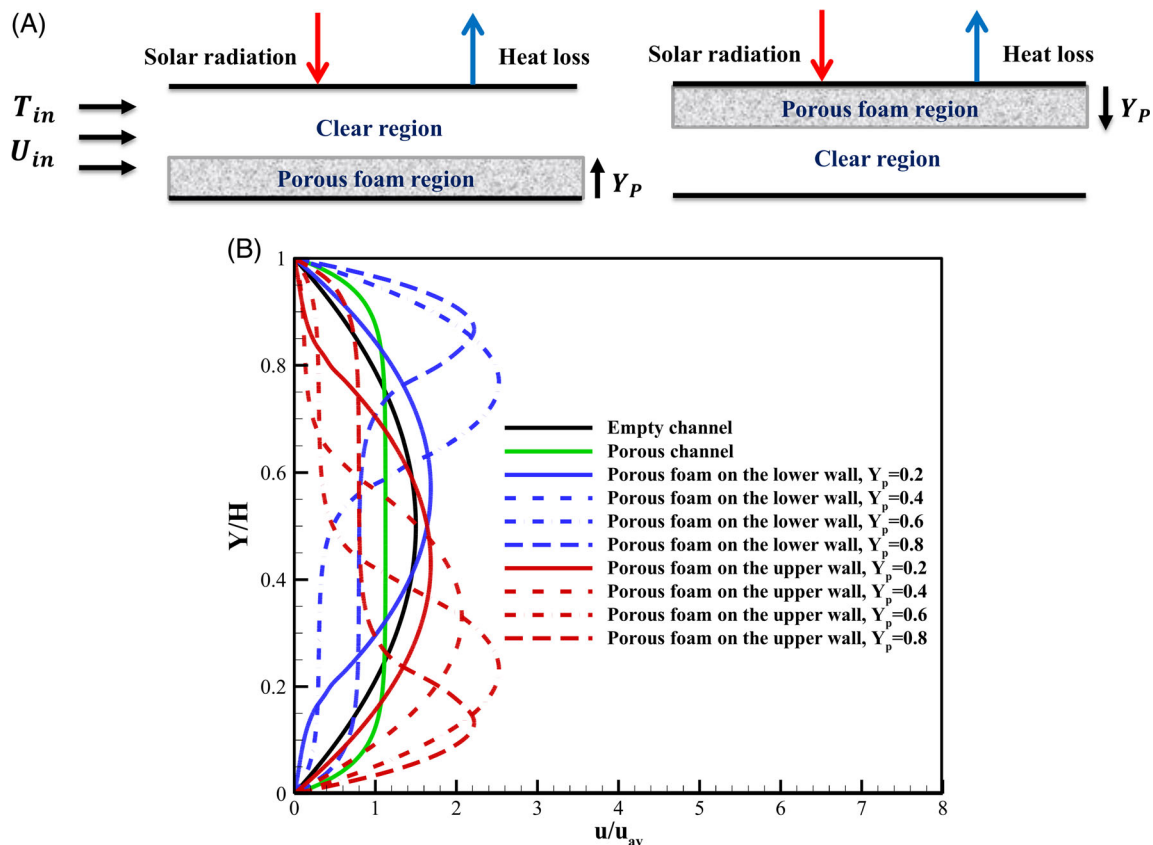


FIGURE 6 (A) Schematic of DACS with metal oxide foam insert on the upper and lower walls. (B) Outlet velocity profile of the DACS for different metal oxide foam thicknesses and insert arrangement [Colour figure can be viewed at wileyonlinelibrary.com]

Figure 5A depicts the entropy generation number for different nanofluid concentrations and mass flow rates. The figure reveals that the entropy generation for all mass flow rates dramatically decreases by increasing the volume fraction of nanoparticles from 0% to 0.01% and the entropy generation increases beyond 0.01% volume fraction. The entropy generation reduction in the volume fraction of 0.01% can be related to the uniform temperature distribution in the collector, which reduces the temperature gradient in this volume fraction. A decreasing-increasing trend in entropy generation variations is also recently reported by Tong et al⁷⁶ who experimentally analyzed the entropy generation of CuO nanofluid flow in a FPSC. By varying the volume fraction from 0.01% to 0.1%, the solar energy absorption in the nanofluid increases, resulting in an increase in entropy generation due to heat transfer irreversibility. As shown in Figure 5A, the entropy generation declines with increasing mass flow rate. The reduction of entropy generation in water flow is greater than in nanofluid flow. The reason is that by increasing the nanoparticle volume fraction, the entropy generation due to friction increases and that due to heat transfer decreases. Since the nanoparticle concentration used in DACS is small, the decreasing effect of entropy generation due to heat transfer

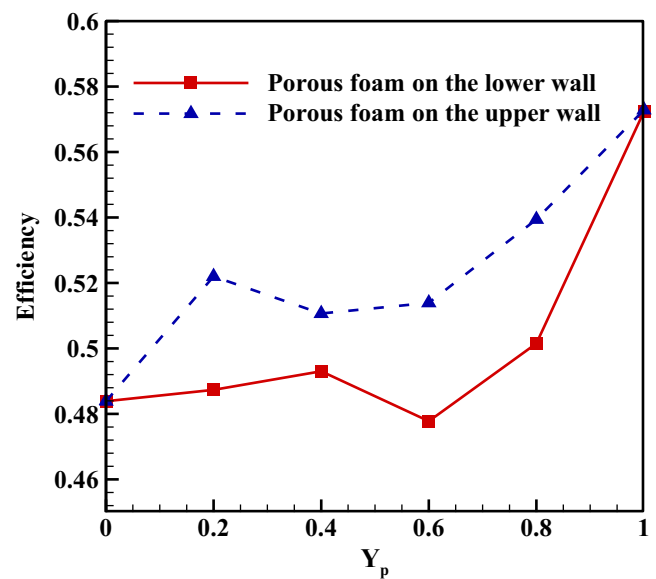


FIGURE 7 Collector efficiency at different metal oxide foam thicknesses and insert arrangements [Colour figure can be viewed at wileyonlinelibrary.com]

overcomes the increasing effect of entropy generation due to friction. Thus, the total entropy value is slightly reduced. To investigate the contribution of entropy

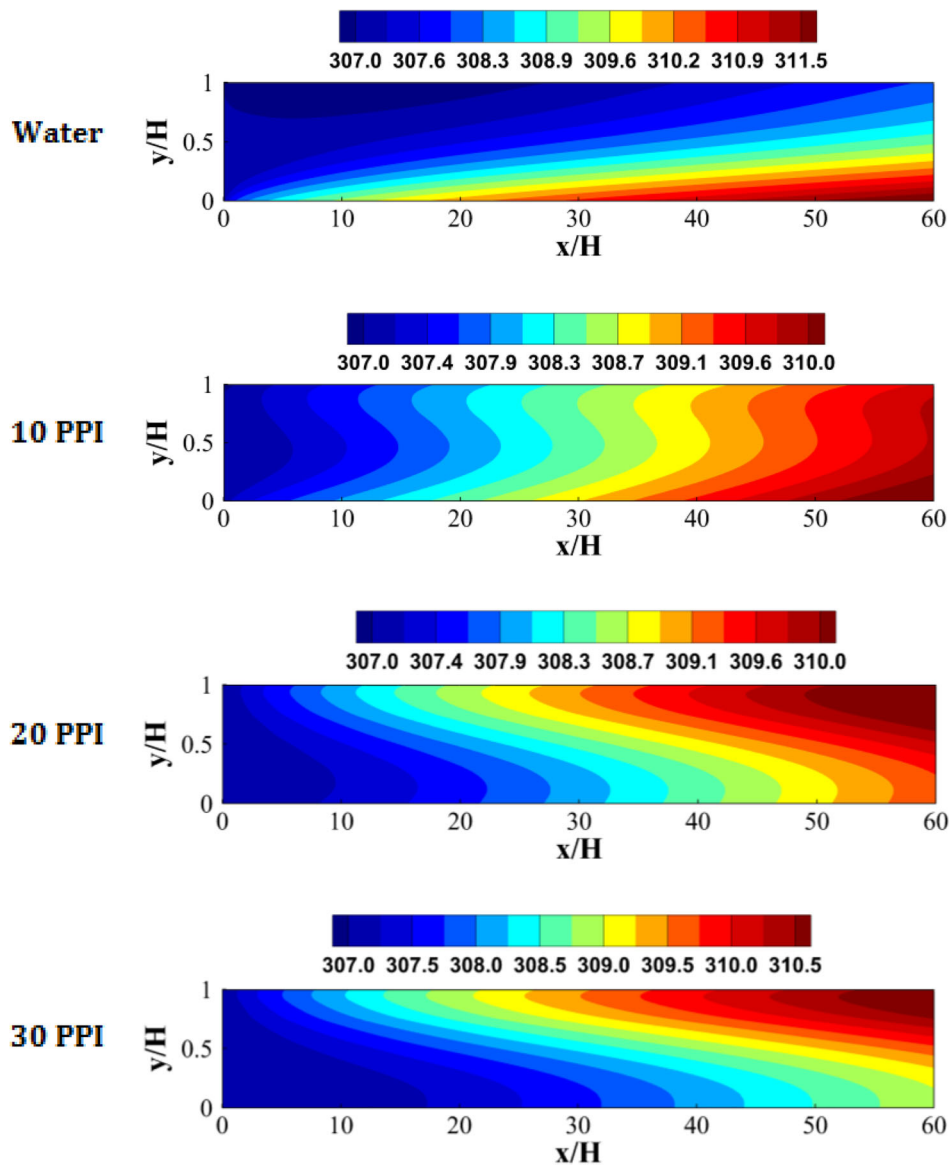


FIGURE 8 Temperature contour for different pore diameters (0.015 kg/s) [Colour figure can be viewed at wileyonlinelibrary.com]

generation resulting from temperature difference in total entropy generation, the Bejan number for different values of the nanoparticle volume fraction and nanofluid mass flow rate is presented in Figure 5B. As shown, as the mass flow rate rises, the proportion of entropy generated by heat transfer to the total entropy generation decreases. Also, as mentioned earlier, at a volume fraction of 0.01%, the temperature distribution becomes more uniform and the temperature gradient drops. Therefore, the minimum amount of Bojan number corresponds to this nanoparticle volume fraction.

3.3 | Performance of DASC filled with CuO porous foam

In this section, the water flow through DASC completely/partially filled with CuO porous foam is

studied. Two typical configurations are considered to investigate the effect of the thickness of porous foam placed on the collector.⁵⁵ In the first case (case 1), the porous foam layer is placed adjacent to the top wall and in the second case (case 2), the metal oxide foam is added to the bottom wall. Figure 6A schematically shows the two cases in which the dimensionless quantity Y_p is the ratio of the thickness of porous foam layer to the collector height. Figure 6B shows the dimensionless fully developed velocity distribution at the collector outlet for two configurations and different values of porous foam thickness. As noticed, the calculations are performed for a mass flow rate of 0.0075 kg/s, a solar radiation flux of 800 W/m² and a foam pore diameter of 30 PPI. As the thickness of porous foam layer increases (for both cases), due to the resistance of the porous foam to the fluid flow, a greater portion of the flow is driven to the clear region, thus increasing the velocity gradient and maximum

velocity in this region. The effect of carrier fluid mass flow rate and porous foam thickness (for both cases) on collector efficiency is demonstrated in Figure 7. As shown, the collector efficiency is higher when the porous foam is located on the upper wall (case 2) compared with the case it is attached to the lower wall (case 1). One notes that the solar radiation absorber is closer to the high-temperature region in the second case than in the first one. As depicted in Figure 7, the collector efficiency for case 1 slowly rises when the porous layer thickness

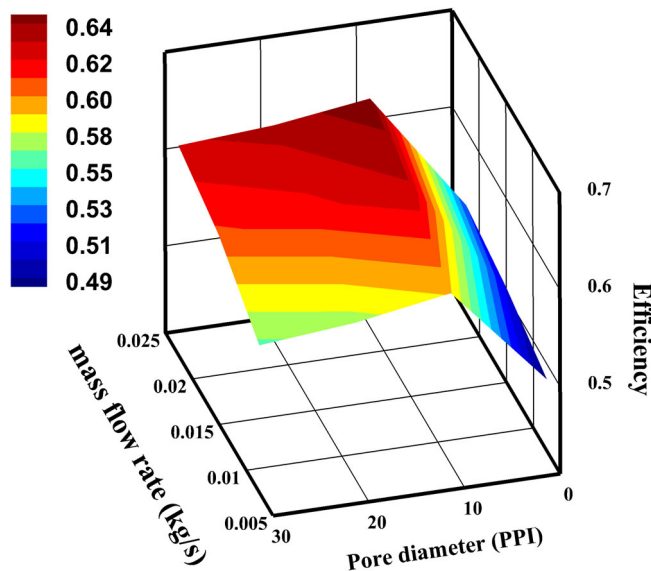


FIGURE 9 Collector efficiency for different pore diameters and mass flow rates [Colour figure can be viewed at wileyonlinelibrary.com]

varies from 0 to 0.4, then suddenly falls to reach a minimum value at $Y_p = 0.6$. Finally, it sharply increases until it maximizes at $Y_p = 1$. For case 2, the collector efficiency increases until $Y_p = 0.2$, stabilizes from 0.2 to 0.6 and dramatically increases to reach a peak value at $Y_p = 1$. The effect of varying the foam pore size on the temperature distribution in DASC fully filled with porous foam at a mass flow rate of 0.015 kg/s is shown in Figure 8. As discussed by Valizade et al,⁵² by decreasing the foam cell number at a given distance (ie, increasing PPI), the light path is shorter and the collision of light with surfaces increases, hence the metal oxide foam absorption coefficient rises. As shown in Figure 8, regarding the water flow in DASC, the incoming radiation to the collector easily penetrates into the water, which is then absorbed by the lower wall and forms a high-temperature zone adjacent to the wall. On the contrary, in the channel filled with metal oxide foam with PPI = 10, the incoming radiation is absorbed by the water-saturated metal oxide foam. Hence, the temperature profile in this case seems more uniform. Decreasing the cell diameter from 10 to 30 PPI results in a growth in the absorption coefficient of water-saturated metal oxide foam. Thus, the incoming solar radiation to the collector is absorbed by fluid upper layers and a high-temperature zone nearby to the upper wall is formed. Figure 9 provides information on the collector efficiency for different foam cell diameters and carrier fluid mass flow rates. One notices that in a porous foam-filled collector, similar to the nanofluid flow, the fluid absorbs more solar radiation with increasing mass flow rate and the collector efficiency rises. Moreover, as the porous pore diameter is altered from 0 to 10 PPI, the

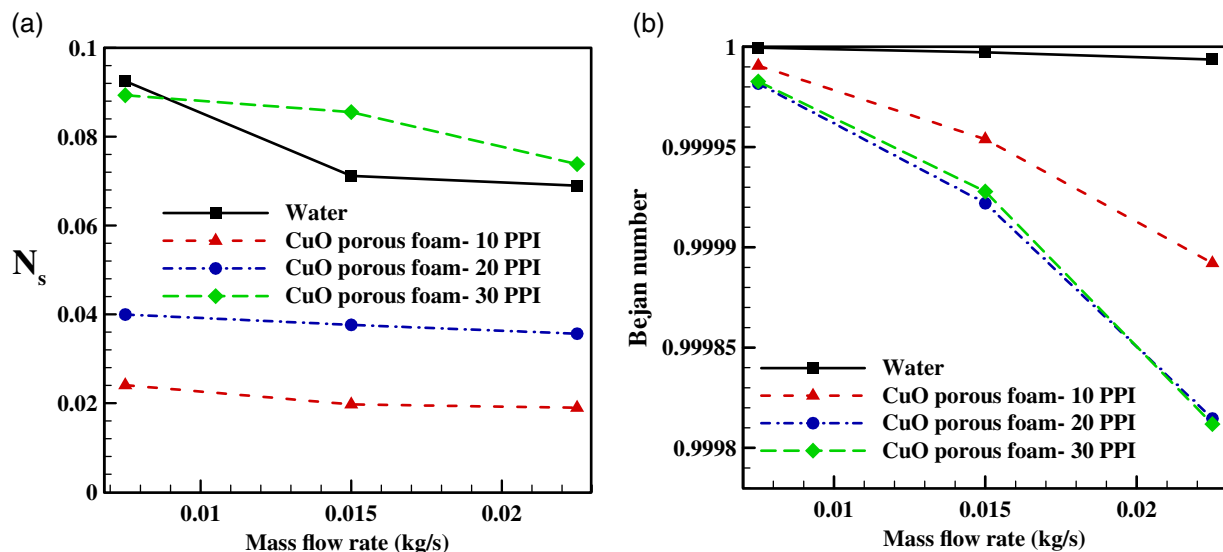


FIGURE 10 (A) Entropy generation number and (B) Bejan number for different pore diameters and mass flow rates [Colour figure can be viewed at wileyonlinelibrary.com]

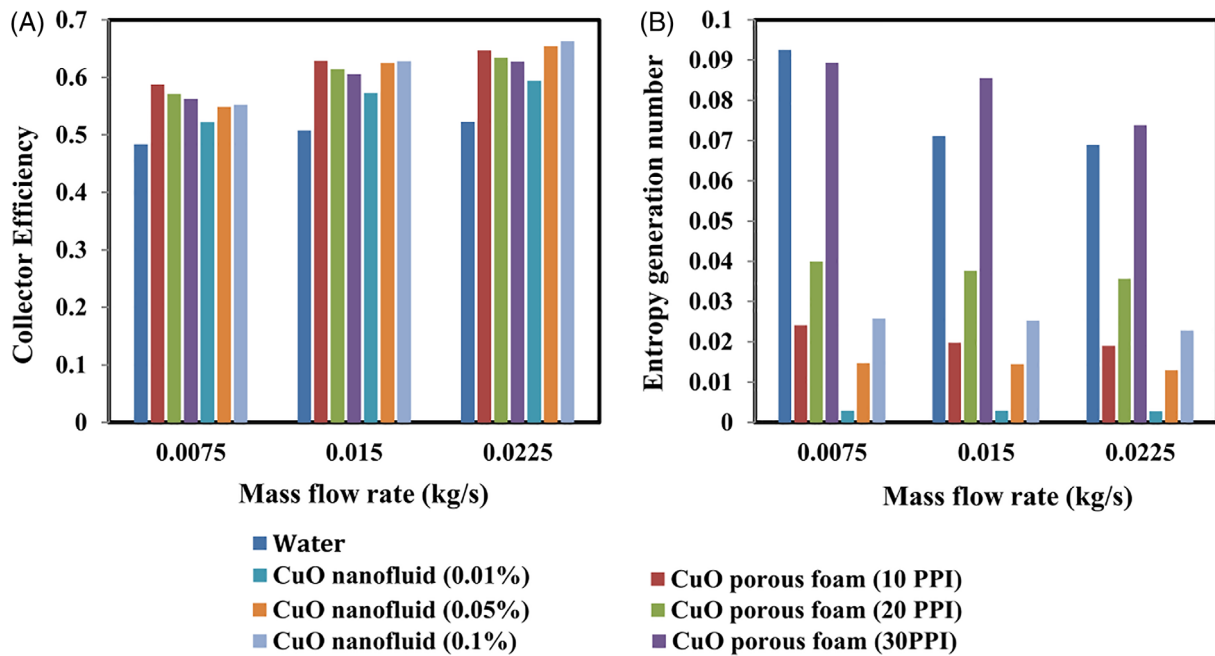


FIGURE 11 (A) Collector efficiency and (B) entropy generation number for different foam pore diameters and nanofluid volume fractions [Colour figure can be viewed at wileyonlinelibrary.com]

collector efficiency significantly rises such that the efficiency improvement for the mass flow rates 0.0075, 0.0015, and 0.025 kg/s are, respectively, 21.3%, 23.7%, and 23.8%. By reducing the cell diameter from 10 to 30 PPI, the collector efficiency decreases. Accordingly, the efficiency graph has a maximum value at the pore diameter of 10 PPI, attributed to the formation of a high-temperature zone near the upper wall and increasing the thermal loss by decreasing the foam cell diameter. Figure 9 also shows that since the temperature profile loses its uniformity with increasing number of pores (10–30 PPI), and the average temperature is used to calculate the collector efficiency, the temperature for the pore diameter of 10 PPI is less than that for 20 and 30 PPI. One should also note that for the nanofluid flow in DASC, as the nanofluid concentration increases, the uniformity of the temperature profile decreases. However, the mean temperature is also slightly increased, hence no local maximum is observed in the efficiency curve of this flow. Figure 10A,B illustrates the variations of entropy generation and Bejan numbers with respect to the water mass flow rate and foam cell diameter. By decreasing the temperature gradient in the metal oxide foam with a pore diameter of 10 PPI, the entropy generation for all mass flow rates dramatically drops. As the foam cell number and, accordingly, the absorption coefficient increase, the irreversibility due to temperature gradient increases, resulting in an upward trend in total entropy generation. Furthermore, as presented in Figure 10B, when the mass flow rate rises, the

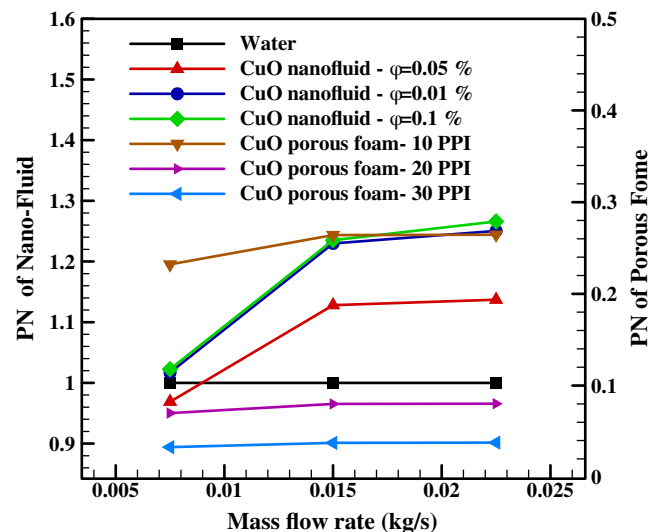


FIGURE 12 PN values of the nanofluid and metal oxide foam versus mass flow rate for different pore diameters and nanofluid volume fractions [Colour figure can be viewed at wileyonlinelibrary.com]

irreversibility due to friction increases and the contribution of heat transfer in the total entropy generation is reduced, causing a downward trend in the Bejan number. Also, by placing the metal oxide foam in the collector, the flow resistance and friction loss are increased, leading to a decline in the Bejan number. By decreasing the foam cell diameter from 20 to 30 PPI, the role of increasing entropy generation as a result of heat transfer becomes

greater than that due to friction. Consequently, a slight increase in the Bejan number variation is observable.

3.4 | Comparison of performance of DASC filled with CuO porous foam and nanofluid

In this section, the use of CuO nanoparticles and foams as the radiation absorbers in DASC is compared. The bar chart in Figure 11A gives information on the DASC efficiency for different CuO nanoparticle volume fractions (0.01%, 0.05%, and 0.1%) and foam pore diameters (10, 20, and 30 PPI) at three various mass flow rates. As observed, the highest efficiency improvement (in comparison to water) at the mass flow rates of 0.0075, 0.015, and 0.0225 kg/s are, respectively, 21% (pore diameter of 10 PPI), 23.8% (pore diameter of 10 PPI and nanoparticle volume fraction of 0.1%), and 26.8% (nanoparticle volume fraction of 0.1%). Overall, a slight change in the collector efficiency occurs after increasing the volume fraction of CuO nanoparticles from 0.05% to 1%, while a reduction in the collector efficiency can be seen after increasing the pore number from 10 to 20 PPI. Thus, the use of CuO nanoparticles with the volume fraction of 0.05% and CuO porous foam with the pore diameter of 10 PPI can be effective in the considered DASC. The collector performance is already examined from the viewpoint of the first law of thermodynamics, as shown in Figure 11A. To evaluate this feature from the second law of thermodynamics standpoint, the entropy generation number is outlined in Figure 11B for different nanofluids volume fractions and number of holes in metal oxide foam. As shown, the total entropy generation for the water-saturated metal oxide foam flow is higher than that for nanofluid flow due to its greater mechanical entropy generation. This can be deduced from the comparison of Equations 16 and 17. Due to the low concentration of nanoparticles used in DASCs, nanofluid viscosity slightly increases with increasing nanoparticle volume fraction. However, the rise in the number of pores in metal oxide foams decreases the porous media permeability and the second term in Equation 17 considerably grows. The maximum entropy generation at the mass flow rate of 0.0075 kg/s belongs to the water flow, while it belongs to the water-saturated metal oxide foam flow with the pore diameter of 30 PPI at the mass flow rates of 0.015 and 0.025 kg/s. Based on the first and second laws of thermodynamics, for an ideal collector, higher efficiency and lower entropy generation are desired. In order to simultaneously investigate the effect of entropy generation and efficiency variations in a DASC

equipped with radiation absorbers, a performance number is defined as.

$$PN = \frac{\eta/\eta_b}{N_{s,F}/(N_{s,F})_b}, \quad (27)$$

where the subscript b represents the base state corresponding to the water flow through DASC in the present study. Due to the importance of pressure drop in solar collectors, the entropy generation as a result of friction ($N_{s,F}$) is used in the denominator of Equation 27. Increasing the efficiency and decreasing the pressure drop relative to the base state improves this parameter. Figure 12 shows the calculated performance number for the nanofluid and metal oxide foam at different working fluid mass flow rates. As observed, for every mass flow rate and pore diameter of the metal oxide foam, the performance number is smaller than unity. This indicates that increased thermal efficiency using metal oxide foams cannot offset the influence of increased mechanical entropy generation. Evidently, in the case of CuO nanofluids, with the exception of 0.05% volume fraction at the mass flow rate of 0.0075 kg/s, the collector performance number in other conditions is greater than one. Furthermore, due to the slight change in the performance number with increasing volume fraction from 0.05% to 0.1%, using nanofluids with the volume fraction of 0.05% is seemingly more advantageous. The maximum performance number for the CuO nanofluid and metal oxide foam corresponds to the volume fraction of 0.1% at the mass flow rate of 0.0225 kg/s and pore diameter of 10 PPI.

4 | CONCLUSION

The current article demonstrated different aspects of thermal performance and entropy generation in a residential-type DASC partially/fully filled with CuO porous foam or occupied by CuO nanofluid using a numerical approach. The finite volume-based numerical simulations were performed to evaluate the effect of nanoparticle volume fraction (0.01%, 0.05%, and 0.01%) and foam pore size (10, 20, and 30 PPI). In both sets of computations, the working fluid mass flow rate was varied from 0.0075 to 0.0225 kg/s and the solar radiation flux was set to 800 W/m². By carefully examining the effect of different parameters, the following results were obtained:

- The numerical solutions were validated against three different experimental and numerical studies and good agreement was obtained. This ensured that the

numerical solver accurately simulated the flow of volumetric participating media in a DASC.

- By increasing the CuO nanoparticle volume fraction, the collector efficiency rapidly rose from 0% to 0.01%, yet it partially increased from 0.05% to 0.1%.
- By increasing the foam layer thickness, the amount of radiation-absorbing medium in the collector increased and an overall rise in collector efficiency was observed.
- When the number of pores were varied from zero (water) to 10 PPI, the collector efficiency increased, and then decreased slightly with the increasing number of pores from 10 to 30 PPI.
- The entropy generation for the DASC filled by metal oxide foam was significantly higher than that for nanofluid flow. In view of the first and second laws of thermodynamics, it was concluded that using nanofluids in the collector is more effective than using metal foams.

ORCID

Mostafa Esmaili  <https://orcid.org/0000-0001-5106-3616>

Maryam Karami  <https://orcid.org/0000-0003-4771-2446>

REFERENCES

- Bhalla V, Tyagi H. Parameters influencing the performance of nanoparticles-laden fluid-based solar thermal collectors: a review on optical properties. *Renew Sustain Energy Rev.* 2018; 84:12-42.
- Nasrin R, Parvin S, Alim MA. Heat transfer and collector efficiency through a direct absorption solar collector with radiative heat flux effect. *Numer Heat Tr A Appl.* 2015;68(8): 887-907.
- Besheer AH, Smyth M, Zacharopoulos A, Mondol J, Pugsley A. Review on recent approaches for hybrid PV/T solar technology. *Int J Energy Res.* 2016;40(15):2038-2053.
- Di Rosa D, Wanic M, Fal J, Żyła G, Mercatelli L, Sani E. Optical and dielectric properties of ethylene glycol-based nanofluids containing nanodiamonds with various purities. *Powder Technol.* 2019;356:508-516.
- Dugaria S, Bortolato M, Del Col D. Modelling of a direct absorption solar receiver using carbon based nanofluids under concentrated solar radiation. *Renew Energy.* 2018;128: 495-508.
- Duan H, Tang L, Zheng Y, Xu C. Effect of plasmonic nanoshell-based nanofluid on efficiency of direct solar thermal collector. *Appl Therm Eng.* 2018;133:188-193.
- Gorji TB, Ranjbar A. Geometry optimization of a nanofluid-based direct absorption solar collector using response surface methodology. *Sol Energy.* 2015;122:314-325.
- Hatami M, Mosayebidorcheh S, Jing D. Thermal performance evaluation of alumina-water nanofluid in an inclined direct absorption solar collector (IDASC) using numerical method. *J Mol Liq.* 2017;231:632-639.
- Ladjevardi S, Asnaghi A, Izadkhash P, Kashani A. Applicability of graphite nanofluids in direct solar energy absorption. *Sol Energy.* 2013;94:327-334.
- Parvin S, Nasrin R, Alim M. Heat transfer and entropy generation through nanofluid filled direct absorption solar collector. *Int J Heat Mass Tran.* 2014;71:386-395.
- Qin C, Kang K, Lee I, Lee BJ. Optimization of a direct absorption solar collector with blended plasmonic nanofluids. *Sol Energy.* 2017;150:512-520.
- Sharaf OZ, al-Khateeb AN, Kyritsis DC, Abu-Nada E. Direct absorption solar collector (DASC) modeling and simulation using a novel Eulerian-Lagrangian hybrid approach: optical, thermal, and hydrodynamic interactions. *Appl Energy.* 2018; 231:1132-1145.
- Sharaf OZ, al-Khateeb AN, Kyritsis DC, Abu-Nada E. Energy and exergy analysis and optimization of low-flux direct absorption solar collectors (DASCs): balancing power-and temperature-gain. *Renew Energy.* 2019;133:861-872.
- Sharaf OZ, Kyritsis DC, Abu-Nada E. Impact of nanofluids, radiation spectrum, and hydrodynamics on the performance of direct absorption solar collectors. *Energy Convers Manage.* 2018; 156:706-722.
- Sharaf OZ, Kyritsis DC, al-Khateeb AN, Abu-Nada E. Effect of bottom surface optical boundary conditions on nanofluid-based DASC: parametric study and optimization. *Sol Energy.* 2018; 164:210-223.
- Siavashi M, Ghasemi K, Yousofvand R, Derakhshan S. Computational analysis of SWCNH nanofluid-based direct absorption solar collector with a metal sheet. *Sol Energy.* 2018;170:252-262.
- Tyagi H, Phelan P, Prasher R. Predicted efficiency of a low-temperature nanofluid-based direct absorption solar collector. *J Sol Energy Eng.* 2009;131(4):041004.
- Delfani S, Karami M, Akhavan-Behabadi M. Performance characteristics of a residential-type direct absorption solar collector using MWCNT nanofluid. *Renew Energy.* 2016;87:754-764.
- Gorji TB, Ranjbar A. Thermal and exergy optimization of a nanofluid-based direct absorption solar collector. *Renew Energy.* 2017;106:274-287.
- Gorji TB, Ranjbar AA. A numerical and experimental investigation on the performance of a low-flux direct absorption solar collector (DASC) using graphite, magnetite and silver nanofluids. *Sol Energy.* 2016;135:493-505.
- Gupta HK, Agrawal GD, Mathur J. An experimental investigation of a low temperature Al₂O₃-H₂O nanofluid based direct absorption solar collector. *Sol Energy.* 2015;118:390-396.
- Gupta HK, Agrawal GD, Mathur J. Investigations for effect of Al₂O₃-H₂O nanofluid flow rate on the efficiency of direct absorption solar collector. *Case Stud Therm Eng.* 2015;5:70-78.
- Karami M. Experimental investigation of first and second laws in a direct absorption solar collector using hybrid Fe₃O₄/SiO₂ nanofluid. *J Therm Anal Calorim.* 2019;136(2):661-671.
- Karami M, Akhavan-Bahabadi MA, Delfani S, Raisee M. Experimental investigation of CuO nanofluid-based direct absorption solar collector for residential applications. *Renew Sustain Energy Rev.* 2015;52:793-801.
- Karami M, Bozorgi M, Delfani S, Akhavan-Behabadi MA. Empirical correlations for heat transfer in a silver nanofluid-based direct absorption solar collector. *Sustain Energy Technol Assess.* 2018;28:14-21.

26. Otanicar TP, Phelan PE, Prasher RS, Rosengarten G, Taylor RA. Nanofluid-based direct absorption solar collector. *J Renew Sustain Energy*. 2010;2(3):033102.
27. Vakili M, Hosseinalipour SM, Delfani S, Khosrojerdi S, Karami M. Experimental investigation of graphene nanoplatelets nanofluid-based volumetric solar collector for domestic hot water systems. *Sol Energy*. 2016;131:119-130.
28. Delfani S, Esmaeili M, Karami M. Application of artificial neural network for performance prediction of a nanofluid-based direct absorption solar collector. *Sustain Energy Technol Assess*. 2019;36:100559.
29. Gorji TB, Ranjbar A. A review on optical properties and application of nanofluids in direct absorption solar collectors (DASCs). *Renew Sustain Energy Rev*. 2017;72:10-32.
30. Karami M, Delfani S, Esmaeili M. Effect of V-shaped rib roughness on the performance of nanofluid-based direct absorption solar collectors. *J Therm Anal Calorim*. 2019;138(1):559-572.
31. Raj P, Subudhi S. A review of studies using nanofluids in flat-plate and direct absorption solar collectors. *Renew Sustain Energy Rev*. 2018;84:54-74.
32. Moradi A, Sani E, Simonetti M, Francini F, Chiavazzo E, Asinari P. Carbon-nanohorn based nanofluids for a direct absorption solar collector for civil application. *J Nanosci Nanotechnol*. 2015;15(5):3488-3495.
33. Rashidi S, Esfahani JA, Rashidi A. A review on the applications of porous materials in solar energy systems. *Renew Sustain Energy Rev*. 2017;73:1198-1210.
34. Anirudh K, Dhinakaran S. Performance improvement of a flat-plate solar collector by inserting intermittent porous blocks. *Renew Energy*. 2020;145:428-441.
35. Chen C-C, Huang P-C. Numerical study of heat transfer enhancement for a novel flat-plate solar water collector using metal-foam blocks. *Int J Heat Mass Tran*. 2012;55(23-24):6734-6756.
36. Hirasawa S, Tsubota R, Kawanami T, Shirai K. Reduction of heat loss from solar thermal collector by diminishing natural convection with high-porosity porous medium. *Sol Energy*. 2013;97:305-313.
37. Jouybari HJ, Saedodin S, Zamzamian A, Nimvari ME. Experimental investigation of thermal performance and entropy generation of a flat-plate solar collector filled with porous media. *Appl Therm Eng*. 2017;127:1506-1517.
38. Jouybari HJ, Saedodin S, Zamzamian A, Nimvari ME, Wongwises S. Effects of porous material and nanoparticles on the thermal performance of a flat plate solar collector: an experimental study. *Renew Energy*. 2017;114:1407-1418.
39. Jouybari HJ, Saedodin S, Zamzamian A, Nimvari ME. Analytical investigation of forced convection heat transfer in a flat-plate solar collector filled with a porous medium by considering radiation effect. *J Porous Media*. 2018;21(12):1177-1195.
40. Saedodin S, Zamzamian SAH, Nimvari ME, Wongwises S, Jouybari HJ. Performance evaluation of a flat-plate solar collector filled with porous metal foam: experimental and numerical analysis. *Energy Convers Manage*. 2017;153:278-287.
41. Lansing F, Clarke V, Reynolds R. A high performance porous flat-plate solar collector. *Energy*. 1979;4(4):685-694.
42. Ghasemi SE, Ranjbar AA. Numerical thermal study on effect of porous rings on performance of solar parabolic trough collector. *Appl Therm Eng*. 2017;118:807-816.
43. Jamal-Abad MT, Saedodin S, Aminy M. Experimental investigation on a solar parabolic trough collector for absorber tube filled with porous media. *Renew Energy*. 2017;107:156-163.
44. Barreto G, Canhoto P, Collares-Pereira M. Three-dimensional modelling and analysis of solar radiation absorption in porous volumetric receivers. *Appl Energy*. 2018;215:602-614.
45. Okonkwo EC, Abid M, Ratlamwala TA. Effects of synthetic oil nanofluids and absorber geometries on the exergetic performance of the parabolic trough collector. *Int J Energy Res*. 2018;42(11):3559-3574.
46. Ray S, Tripathy AK, Sahoo SS, Bindra H. Performance analysis of receiver of parabolic trough solar collector: effect of selective coating, vacuum and semitransparent glass cover. *Int J Energy Res*. 2018;42(13):4235-4249.
47. Bai F. One dimensional thermal analysis of silicon carbide ceramic foam used for solar air receiver. *Int J Therm Sci*. 2010;49(12):2400-2404.
48. Chen X, Xia XL, Meng XL, Dong XH. Thermal performance analysis on a volumetric solar receiver with double-layer ceramic foam. *Energy Convers Manage*. 2015;97:282-289.
49. Wu Z, Caliot C, Flamant G, Wang Z. Coupled radiation and flow modeling in ceramic foam volumetric solar air receivers. *Sol Energy*. 2011;85(9):2374-2385.
50. Tayebi R, Akbarzadeh S, Valipour MS. Numerical investigation of efficiency enhancement in a direct absorption parabolic trough collector occupied by a porous medium and saturated by a nanofluid. *Environ Prog Sustain Energy*. 2019;38(2):727-740.
51. Valizade M, Heyhat M, Maerefat M. Experimental study of the thermal behavior of direct absorption parabolic trough collector by applying copper metal foam as volumetric solar absorption. *Renew Energy*. 2020;145:261-269.
52. Valizade M, Heyhat M, Maerefat M. Experimental comparison of optical properties of nanofluid and metal foam for using in direct absorption solar collectors. *Sol Energy Mater Sol Cells*. 2019;195:71-80.
53. Esmaeili M, Sadeghy K, Moghaddami M. Heat transfer enhancement of wavy channels using Al₂O₃ nanoparticles. *J Enhanc Heat Transf*. 2010;17(2):139-151.
54. Ghazvini M, Akhavan-Behabadi M, Esmaeili M. The effect of viscous dissipation on laminar nanofluid flow in a micro-channel heat sink. *P I Mech Eng C J Mech Eng Sci*. 2009;223(11):2697-2706.
55. Mahdavi M, Saffar-Avval M, Tiari S, Mansoori Z. Entropy generation and heat transfer numerical analysis in pipes partially filled with porous medium. *Int J Heat Mass Tran*. 2014;79:496-506.
56. Ergun S. Fluid flow through packed columns. *Chem Eng Prog*. 1952;48:89-94.
57. Vafai K. *Handbook of Porous Media*. USA: Crc Press; 2015.
58. Vafai K, Kim S. On the limitations of the Brinkman-Forchheimer-extended Darcy equation. *Int J Heat Fluid Fl*. 1995;16(1):11-15.
59. Rahimi-Gorji M, Pourmehran O, Gorji-Bandpy M, Ganji DD. Unsteady squeezing nanofluid simulation and investigation of its effect on important heat transfer parameters in presence of magnetic field. *J Taiwan Inst Chem Eng*. 2016;67:467-475.

60. Kumar S, Tien C. Analysis of combined radiation and convection in a particulate-laden liquid film. *J Sol Energy Eng*. 1990; 112(4):293-300.
61. Bejan A, Kestin J. Entropy generation through heat and fluid flow. *J Appl Mech*. 1983;50:475.
62. Siavashi M, Bahrami HRT, Saffari H. Numerical investigation of flow characteristics, heat transfer and entropy generation of nanofluid flow inside an annular pipe partially or completely filled with porous media using two-phase mixture model. *Energy*. 2015;93:2451-2466.
63. MAXWELL-GARNETT JC. Colours in metal glasses and in metallic films. *Phil Trans R Soc Lond A*. 1904;203:385-420.
64. Brinkman H. The viscosity of concentrated suspensions and solutions. *J Chem Phys*. 1952;20(4):571-571.
65. Einstein A. A new determination of molecular dimensions. *Ann Phys*. 1906;19:289-306.
66. Batchelor G. The effect of Brownian motion on the bulk stress in a suspension of spherical particles. *J Fluid Mech*. 1977;83(1):97-117.
67. Wang X, Xu X, Choi SUS. Thermal conductivity of nanoparticle-fluid mixture. *J Thermophys Heat Tr*. 1999;13(4): 474-480.
68. Chon CH, Kihm KD, Lee SP, Choi SUS. Empirical correlation finding the role of temperature and particle size for nanofluid (Al₂O₃) thermal conductivity enhancement. *Appl Phys Lett*. 2005;87(15):153107.
69. Mints HA, Roy G, Nguyen CT, Doucet D. New temperature dependent thermal conductivity data for water-based nanofluids. *Int J Therm Sci*. 2009;48(2):363-371.
70. Nguyen C, Desgranges F, Roy G, et al. Temperature and particle-size dependent viscosity data for water-based nanofluids—hysteresis phenomenon. *Int J Heat Fluid Fl*. 2007; 28(6):1492-1506.
71. Mliki B, Abbassi MA, Omri A, Zeghmati B. Effects of nanoparticles Brownian motion in a linearly/sinusoidally heated cavity with MHD natural convection in the presence of uniform heat generation/absorption. *Powder Technol*. 2016;295: 69-83.
72. Navaei A, Mohammed H, Munisamy K, Yarmand H, Gharehkhani S. Heat transfer enhancement of turbulent nanofluid flow over various types of internally corrugated channels. *Powder Technol*. 2015;286:332-341.
73. Mohamad A. Heat transfer enhancements in heat exchangers fitted with porous media part I: constant wall temperature. *Int J Therm Sci*. 2003;42(4):385-395.
74. Roache PJ. Perspective: a method for uniform reporting of grid refinement studies. *J Fluids Eng Tr ASME*. 1994;116(3):405-413.
75. Celik IB, Ghia U, Roache PJ, Freitas CJ. Procedure for estimation and reporting of uncertainty due to discretization in CFD applications. *J Fluids Eng Tr ASME*. 2008;130(7):078001.
76. Tong Y, Lee H, Kang W, Cho H. Energy and exergy comparison of a flat-plate solar collector using water, Al₂O₃ nanofluid, and CuO nanofluid. *Appl Therm Eng*. 2019;159:113959.
77. Jafaryar M, Sheikholeslami M, Li Z. CuO-water nanofluid flow and heat transfer in a heat exchanger tube with twisted tape turbulator. *Powder Technol*. 2018;336:131-143.

How to cite this article: Esmaili M, Karami M, Delfani S. Performance enhancement of a direct absorption solar collector using copper oxide porous foam and nanofluid. *Int J Energy Res*. 2020; 1–18. <https://doi.org/10.1002/er.5305>